

Communication

Metal Oxide Nanorods-Based Sensor Array for Selective Detection of Biomarker Gases

Gwang Su Kim ^{1,2}, Yumin Park ^{1,2}, Joonchul Shin ², Young Geun Song ^{2,*} and Chong-Yun Kang ^{1,2,*}

¹ KU-KIST Graduate School of Converging Science and Technology, Korea University, Seoul 02841, Korea; 218307@kist.re.kr (G.S.K.); wsx6659@kist.re.kr (Y.P.)

² Electronic Materials Research Center, Korea Institute of Science and Technology (KIST), Seoul 02791, Korea; spy21318@kist.re.kr

* Correspondence: songyg6397@kist.re.kr (Y.G.S.); cykang@kist.re.kr (C.-Y.K.)

Abstract: The breath gas analysis through gas phase chemical analysis draws attention in terms of non-invasive and real time monitoring. The array-type sensors are one of the diagnostic methods with high sensitivity and selectivity towards the target gases. Herein, we presented a 2×4 sensor array with a micro-heater and ceramic chip. The device is designed in a small size for portability, including the internal eight-channel sensor array. In_2O_3 NRs and WO_3 NRs manufactured through the E-beam evaporator's glancing angle method were used as sensing materials. Pt, Pd, and Au metal catalysts were decorated for each channel to enhance functionality. The sensor array was measured for the exhaled gas biomarkers CH_3COCH_3 , NO_2 , and H_2S to confirm the respiratory diagnostic performance. Through this operation, the theoretical detection limit was calculated as 1.48 ppb for CH_3COCH_3 , 1.9 ppt for NO_2 , and 2.47 ppb for H_2S . This excellent detection performance indicates that our sensor array detected the CH_3COCH_3 , NO_2 , and H_2S as biomarkers, applying to the breath gas analysis. Our results showed the high potential of the gas sensor array as a non-invasive diagnostic tool that enables real-time monitoring.



Citation: Kim, G.S.; Park, Y.; Shin, J.; Song, Y.G.; Kang, C.-Y. Metal Oxide Nanorods-Based Sensor Array for Selective Detection of Biomarker Gases. *Sensors* **2021**, *21*, 1922. <https://doi.org/10.3390/s21051922>

Academic Editor: Elisabetta Comini

Received: 28 January 2021

Accepted: 4 March 2021

Published: 9 March 2021

Publisher's Note: MDPI stays neutral with regard to jurisdictional claims in published maps and institutional affiliations.



Copyright: © 2021 by the authors. Licensee MDPI, Basel, Switzerland. This article is an open access article distributed under the terms and conditions of the Creative Commons Attribution (CC BY) license (<https://creativecommons.org/licenses/by/4.0/>).

Keywords: semiconducting gas sensor; array; nanostructure; metal oxide

1. Introduction

Healthcare is now undergoing a paradigm shift that will transform the nature of medicine from reactive to preventive [1]. The changes are facilitated by a new approach to a disease that will lead to the emergence of personalized medicine that focuses on the nearby environment, treatment, and disease prevention in individual patients [2]. Large-scale healthcare methods, which have relied on waiting for the patient to get sick, will be replaced by personalized, predictive, preventive, and participatory (P4) medicine via the convergence of the approaches to disease, useful measurement, visualization techniques, and new computational tools [3].

Based on these needs, monitoring the harmful gases present in the environment or breathing has been extensively concentrated as a suitable healthcare approach [4]. In general, indoor air quality is contaminated by harmful gases emitted from building materials, furniture, and appliances, which induce dizziness, paralysis, dyspnea and eventually lead to a comatose state [5]. These gases contain a lot of chemical vapors (NO_2 , CO , NH_3 , and volatile organic compounds (VOCs)) at different concentrations ranging from parts per billion (ppb) to parts per million (ppm) [6]. Furthermore, some chemical vapors, by-products of metabolic processes, show apparent correlation with a particular disease and possibly indicate potential diseases such as asthma [7], diabetes [8], liver diseases [9], lung cancer [10], and metabolic disorders [11], working as biomarkers. However, commercial instruments such as gas chromatography-mass spectrometry (GC-MS) and selected ion-flow tube mass spectrometry (SIFT-MS) are too bulky and costly

to use anytime and anywhere [12]. They could also not offer continuous or real-time information regarding the present state of indoor or individual patients [13].

To overcome these drawbacks, many researchers have studied metal oxide semiconductors (MOs) due to their outstanding advantages, such as low cost, simplicity in fabrication, high sensitivity, easy integration with electronic circuits, and a large number of detectable gases [14]. Cutting-edge research has been spotlighted to apply the nanostructured materials [15], catalysts [16], heterojunctions [17], and UV activation [18] to the sensors for the enhancement of gas sensing performance. However, relatively low gas selectivity remains a challenge to be solved [19]. In general, the catalysts, including Au [20], Pt [21], and Pd [22], functionalize the surface of the sensing materials, leading to an enhancement of sensitivity and selectivity via electronic and chemical sensitization, respectively. However, there are limits to classifying various gases with a combination of a single catalyst and metal oxide. For directly comparing and analyzing the role of the catalyst and classifying multiple gases, the sensor array is considered a suitable approach [23].

Herein, we presented a 2×4 sensor array using In_2O_3 and WO_3 nanorods (NRs), decorated with Au, Pt, and Pd utilizing an electron beam evaporator based on our previous reports [24] (In_2O_3 NRs, Au-decorated In_2O_3 NRs, Pt decorated In_2O_3 NRs, Pd decorated In_2O_3 NRs, WO_3 NRs, Au-decorated WO_3 NRs, Pt decorated WO_3 NRs, and Pd decorated WO_3 NRs). We then evaluated the 2×4 array gas sensor with the maximum detection performance through a metal catalyst for detection characteristics at an operating temperature of 150–300 °C toward CH_3COCH_3 , NO_2 , and H_2S , which are representative biomarkers of diabetes, asthma, and halitosis, respectively.

2. Materials and Methods

2.1. Device Fabrication

The sensor array composed of Pt/Ti (80 nm/20 nm thick) interdigitated electrodes (IDEs) was fabricated on a four-inch SiO_2/Si wafer through standard photolithography and lift-off processes. The distances between each electrode were 5 μm , and there were 20 electrodes in a 1 mm \times 0.25 mm area. An electron-beam evaporator was subsequently used to deposit 300 nm-thick In_2O_3 and WO_3 nanostructures on the prepared IDEs at a glancing angle of 80° in off-axis mode. The substrate was placed 30 cm away from the crucible, and the lift-off process was employed to deposit only onto the area containing the electrodes. As a next step, the catalysts, including Pt, Au, and Pd, were evaporated on the metal oxides by electron beam evaporator in on-axis mode. All the fabricated sensor arrays were annealed at 550 °C for 2 h in ambient air to crystallize the metal oxides and agglomerate the catalysts. The annealing temperature was applied considering the trade-off relationship between the sensor stability and gas response. Then, the sensor array consisting of the 2×4 sensor array was mounted on an Ag-based micro-heater and a chip carrier using a silver paste and ceramic bond, respectively.

2.2. Characterization

X-ray diffraction (DMax2500) was used to analyze deposited films with 2θ scan from 20° to 50°, where Cu $K\alpha$ radiation (wavelength; 1.5418 Å) was used for the X-ray source with a fixed incident angle of 2°. The morphology of the fabricated nanostructures was observed using a field-emission scanning electron microscope (SEM) (Inspect F50) with an acceleration voltage of 15 kV and a working distance of 10 mm.

2.3. Sensor Property Measurement

We measured the gas sensing properties of the 2×4 sensor array in a hand-made measuring chamber. The operating temperature was controlled by heating the micro-heater using a programmable power supply (PSH-3620A) and was calibrated using an infrared camera. The gas flow rate of 1000 sccm was maintained using mass-flow controllers. In this condition, the gas was changed from dry air to the calibrated target gas (balanced with dry air). The resistance was measured at a dc bias voltage of 1 V using a source measurement unit (Keithley 2401), and

each sensor was connected using a switch system (Keithley 7001). All the measurements were recorded on a computer using LabVIEW with general purpose interface bus (GPIB).

3. Results and Discussion

Highly porous nanostructured metal oxides have been mainly used as gas sensing materials because of their large surface-to-volume ratio, narrow necks between each grain, and effective gas accessibility. In our previous work [25], the glancing angle deposition (GAD) method was reported to fabricate useful gas sensing materials. As shown in Figure 1a, the 300-nm thick nanorods metal oxide including (In_2O_3 and WO_3) was evaporated on the Pt interdigitated electrodes (IDEs) using the GAD method at a glancing angle of 80° . When depositing the metal oxides, the incident angle of the vapor flux generates the self-shadowing effect, resulting in the highly porous nanostructured materials (Figure 1b). Subsequently, the catalysts, including Au, Pt, and Pd was evaporated on the surface of the metal oxides with different thickness of 1–2 nm (Figure 1c). The Au, Pt, and Pd were deposited under the condition of becoming a uniform 1 or 2 nm-thick film. To reduce the deposition and photolithography sequences, we chose the 2×4 array, which maximizes the sort of gas sensor up to eight sensors. The 2×4 array sensor can drastically reduce the number of deposition and photolithography processes required for sensor fabrication. The identical sensing materials and catalysts are deposited for the vertical and horizontal directions, respectively. All fabricated sensor array was annealing at 550°C for 2 h to crystallize the metal oxides. The catalysts were aggregated to nanoparticles, resulting in the metal oxide NRs decorated with the catalyst nanoparticles on the surface. Subsequently, the 2×4 sensor array was mounted on the Au-based micro-heater for back heating and the chip carrier for electrical connecting (Figure 1d).

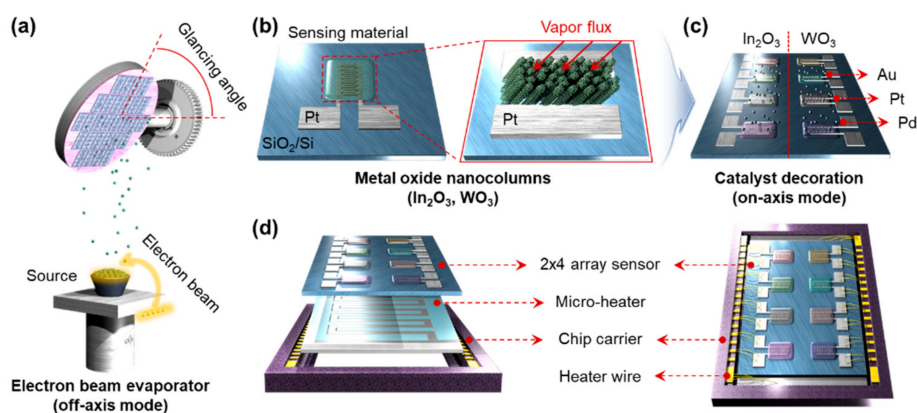


Figure 1. Schematic illustration of (a) the fabrication procedures for porous nanostructures using GAD. (b) A design of Pt-IDEs and metal oxide nanorods grown the direction of the vapor flux. (c) The position of Au, Pt, and Pd catalysts decorated by e-beam evaporator using on-axis mode. (d) 2×4 sensor array with 2×4 sensor array, back heater, chip carrier, and Au wires.

To investigate the morphologies of the sensing materials, the SEM was carried out as shown in Figure 2a–d,f–i. Insets in Figure 2 indicate cross sectional SEM images. The highly porous and well aligned In_2O_3 NRs and WO_3 NRs were observed in Figure 2a,f. When decorating the catalysts on the metal oxide surface, the nano size of nanoparticles was observed in Figure 2 b–d,g–i. XRD in Figure 2e,j characterized the crystallinities of the 2×4 sensors. There is no significant impurity phase from the XRD results, indicating that the In_2O_3 NRs and WO_3 NRs were well crystallized during the annealing process. At the same time, peaks corresponding to Au, Pt, and Pd were not observed. We assume that the peaks corresponding to Au, Pt, and Pd are underneath those corresponding to In_2O_3 and WO_3 because the surface contains less catalyst components. We presented SEM images of a metal catalyst on a SiO_2 substrate. As shown Figure S1, the metal catalysts of Au, Pt, and Pd were clearly deposited on the surface and uniformly dispersed in the form of

nanoparticles on the SiO_2 substrate. Compared with Figure 2 in the manuscript, the metal nanoparticles deposited on the SiO_2 thin film shows relatively large diameter-sizes because of a lower surface energy of the SiO_2 . Therefore, we expected that the metal catalysts were well dispersed on the surface of oxide nanorods with nanosized particles.

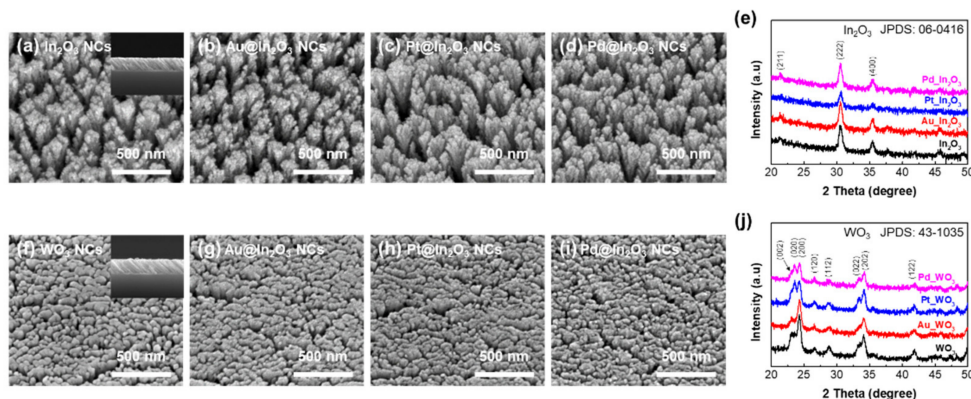


Figure 2. Top-view and cross-sectional (inset) FE-SEM images of (a–d) bare, Au-, Pt-, and Pd-decorated In_2O_3 nanorods, (f–i) bare, Au- (2 nm), Pt- (1 nm), and Pd- (2 nm) decorated WO_3 nanorods. X-ray diffraction pattern of (e) In_2O_3 and (j) WO_3 nanorods as a function of decorated catalysts.

The gas sensing properties of the 2×4 sensor array were measured in the sensing chamber shown in the Figure 3a, and the array signals were acquired simultaneously in real time. We fabricated a measuring chamber for an array. The chamber was sealed with rubber to prevent the inflow of external atmosphere and leakage of the internal measurement atmosphere. The metal oxide-based semiconductor gas sensor has been focused on because of its inexpensiveness, small size, and ease of integration with electronic circuits. However, it requires a high operating temperature of about 200–400 °C to maximize the gas response and accessibility, resulting in high power consumption and poor sensor stability because of thermally induced grain growth. Recently, there are many reports to reduce the operating temperature and the power consumption by miniaturizing the gas sensor. In this regard, we can significantly reduce the power consumption of our array sensor by miniaturizing the chip size. The operating temperature was controlled by back heating the micro-heater. The power consumption of the micro-heater is indicated in Figure 4a. By increasing the power consumption of the micro-heater, the operating temperature linearly increased. Although our micro-heater requires massive power consumption compared to that of the conventional gas sensors, an energy consumption of the heater is sufficiently reduced by miniaturizing the sensor array and decreasing the heating region.

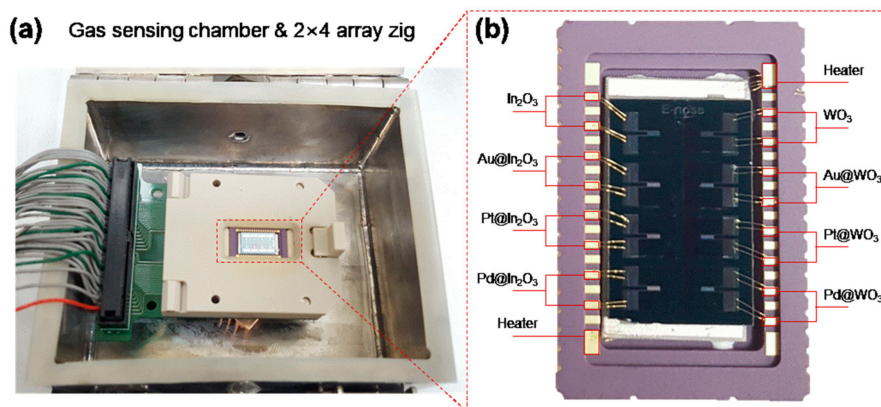


Figure 3. (a) Optical image of the gas sensing chamber and (b) 2×4 sensor array mounted on the micro-heater and the chip carrier.

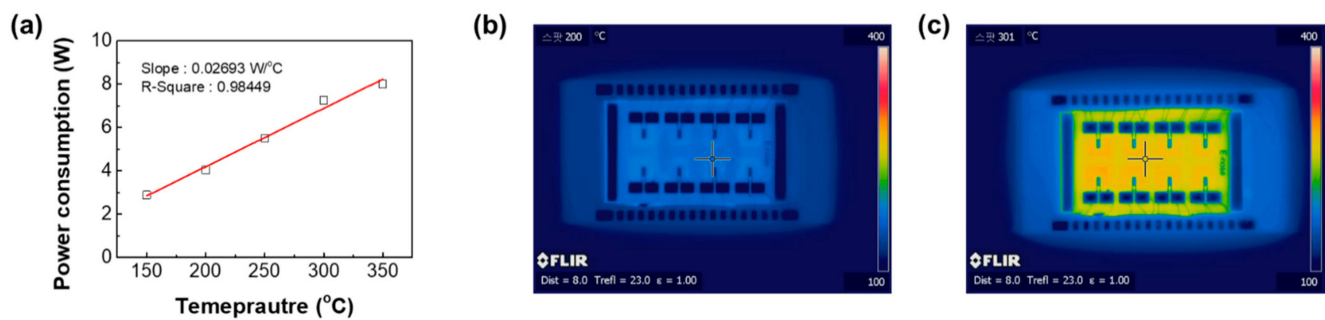


Figure 4. (a) Power consumption of the micro-heater. Infrared images of 2×4 sensor array with different operating temperature; (b) 200 °C and (c) 300 °C.

The sensing properties of the semiconducting gas sensor are highly affected by the operating temperature; with an increase in the temperature, the gas adsorption rate increases due to reduced activation energy with the sensing materials, resulting in the enhancement of the gas response. However, the gas response tends to decrease above a certain temperature since the desorption rate also increases. Therefore, the operating temperature optimization according to the target gases is essential for the semiconducting gas sensors. We selected CH_3COCH_3 , NO_2 , and H_2S as representative biomarkers of diabetes, asthma, and halitosis, respectively [26]. Figure 5a–c show the 2×4 sensors' response to CH_3COCH_3 , NO_2 , and H_2S gas over a temperatures range of 150–350 °C with a setting span of 50 °C for the precise temperature classification and efficient experimentation. The slight modulation of gas flow rate can influence on the operating temperature although a constant flow rate was set to 1000 sccm in this experiment. However, the base resistances of all sensors are not significantly changed for the measurement, indicating that the operating temperature is identical or is less affected by the slight modulation of flow rate. The response of the sensor is defined as $R_a/R_g - 1$ in reducing gas and $R_g/R_a - 1$ in oxidizing gas, depending on the gas type [27]. R_a indicates the sensor resistance in the absence of gas, and R_g denotes the resistance in the presence of target gas. In the case of CH_3COCH_3 , the overall detection performance was excellent at 300 °C, and Au-decorated In_2O_3 NRs and Pt-decorated In_2O_3 showed the highest response compared to other sensors (Figure 5a). On the other hand, NO_2 shows the highest detection performance at 150 °C, and Au-decorated In_2O_3 NRs show the highest response (Figure 5b). For H_2S , Au-decorated WO_3 NRs showed high detection characteristics at 250 °C (Figure 5c). The optimized temperature for the gas sensors is determined by the adsorption as mentioned above and desorption rates depending on the target gas. Moreover, the oxygen species on the surface of the metal oxide can affect the optimum temperature. With increasing the temperature, the negatively charged oxygen species are generated. It is known that the ionosorption (O_2^-) of physisorbed oxygen is formed at more than 100 °C. Subsequently, the oxygen is chemisorbed on the surface as a form of O^- up to 350 °C. Above the temperature of 350 °C, O_2^- is generated by extracting the electrons from the metal oxides. Based on these reactions, NO_2 competes with O_2 to adsorb on the metal oxide surface, indicating a lower response at a high operating temperature [28]. In contrast, the reducing gases involving CH_3COCH_3 and H_2S show a higher response at high temperature. Therefore, we adopted optimum temperatures of 300, 150, and 250 °C towards CH_3COCH_3 , NO_2 , and H_2S , respectively. The high response of our sensor array was elucidated by utility factor, transducer function, and receptor function. The narrow necks between each NRs can enhance the response to target gas (Figure 5d), and the high porosity enables effective target gas accessibility (Figure 5e) [29]. The use of catalysts in the gas sensors has been considered as a promotor of gas adsorption by a spill-over effect (Figure 5f) [30].

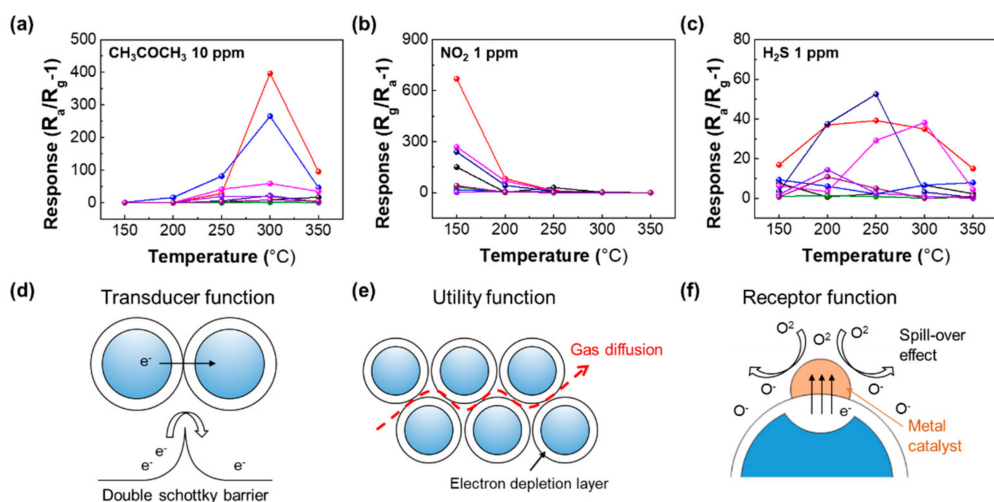


Figure 5. Response of the 2×4 sensor array to (a) 10 ppm CH_3COCH_3 , (b) 1 ppm NO_2 , and (c) H_2S 1 ppm vs. the wide range of operating temperatures from 150 to 350 °C. (d) Transducer function, (e) utility function, and (f) receptor function and spill-over effect that represent gas mechanisms.

To examine the response linearity and detection limit of our sensor, we exposed the 2×4 sensor array to 100–500 ppb CH_3COCH_3 , NO_2 , and H_2S at the operating temperatures of 300, 150, and 250 °C, respectively. As mentioned above, the gas sensing properties were evaluated at the optimum temperatures depending on the target gas. The Figure 6a–c shows response transients of eight sensors. Based on these results, the responses are plotted in Figure 6d–f. Upon exposure to target gases, the responses linearly increase with increasing the gas concentration. Although the 100 ppb was the lowest concentration examined experiment in the study, the theoretical detection limits (signal-to-noise ratio > 3) are calculated to be 1.48 ppb, 1.90 ppt, and 2.47 ppb toward CH_3COCH_3 , NO_2 , and H_2S , respectively. The following result refers to the potential of the gas sensor array, which can trace the meager difference of the gas concentration.

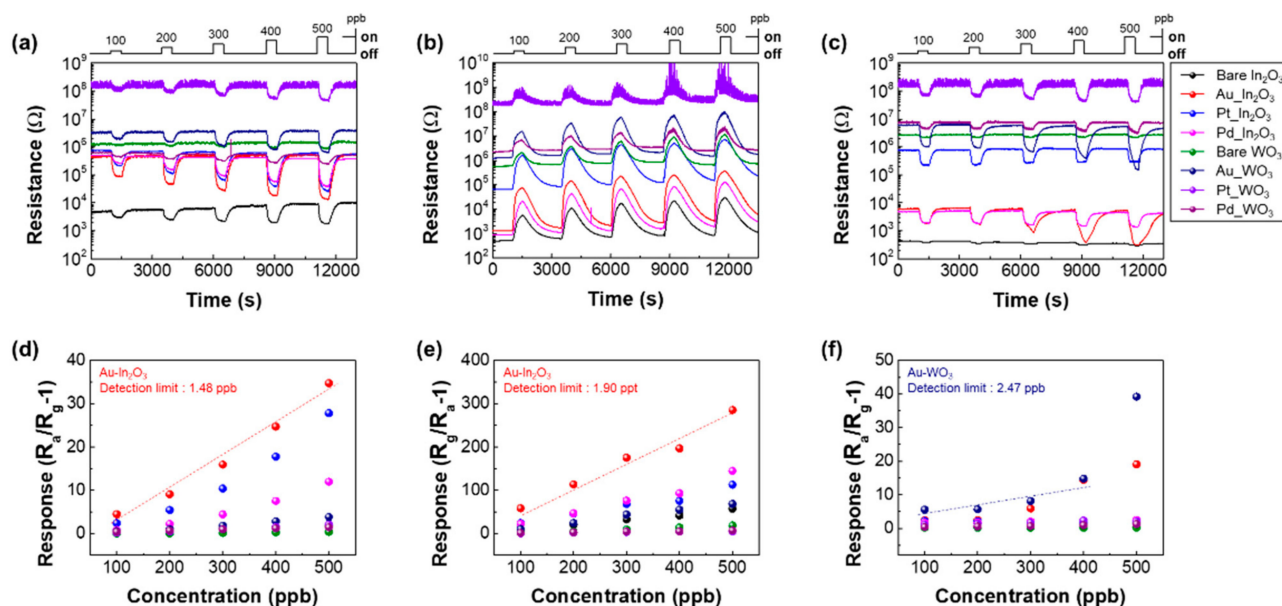


Figure 6. Response of the 2×4 sensor array to 100–500 ppb (a) CH_3COCH_3 , (b) NO_2 , and (c) H_2S at 300 °C, 150 °C, and 250 °C, respectively. Theoretical detection of limit of 2×4 sensor array to 100–500 ppb (d) CH_3COCH_3 , (e) NO_2 , and (f) H_2S .

In a semiconducting gas sensor, it is difficult to clearly realize gas selectivity because the characteristics of the sensor vary depending on the combination of catalyst and metal oxide, the morphology of the nanostructure, and the deposition method.

To clearly demonstrate the selectivity of our sensor array, we plotted the polar plots. Figure 7 shows the response of 2×4 array sensor to CH_3COCH_3 10 ppm, NO_2 1 ppm, and H_2S 1 ppm at the optimized temperature (300, 150, and 250 °C). For the Figure 7a,b, the single target detection of CH_3COCH_3 and NO_2 was clearly observed because both gases are highly dependent on the temperature (Figure 5a,b). Furthermore, the selective detection at 250 °C in Figure 7c is achieved by different patterns with each target gas.

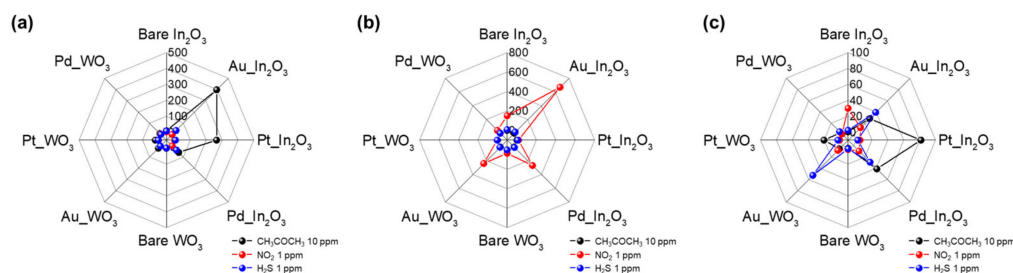


Figure 7. Polar plot of 2×4 array sensor responses of (a) 10 ppm CH_3COCH_3 , (b) 1 ppm NO_2 , and (c) 1 ppm H_2S at the operating temperatures of 300, 150, and 250 °C.

To develop our sensor array for medical applications, it is necessary to investigate the effect of water molecules on the gas sensing properties because of high relative humidity in exhaled gas [31]. In addition, it is reported that the exhaled gas contains a myriad of volatile organic compounds (VOCs), which hinders single target detection of a biomarker [32]. Therefore, we plan to improve the gas selectivity using deep learning-based data analysis and precise analysis, including primary component analysis (PCA) [33], factor analysis (FA) [34], and cluster analysis (CA) [35].

4. Conclusions

In the recent healthcare market, a portable diagnostic device can reduce the inconvenience of visiting a hospital for disease prevention and diagnosis. [36] The electronic nose, which diagnoses diseases by detecting biomarkers in exhaled gas, is being studied as a promising candidate. [37] In this study, we developed an array gas sensor device based on nanostructured metal oxide sensing materials. The device consists of a 2×4 array gas sensor with eight channels, a micro-heater, and a ceramic chip. We measured the fabricated 2×4 array gas sensor for CH_3COCH_3 , NO_2 , and H_2S gases, known as biomarkers for human disease. As a result of the measurements, the 2×4 array gas sensor showed high detection performance at sub ppb level for target gases and showed excellent recovery and repeatability. Moreover, each channel, separated by a metal catalyst, presented different detection performance according to the measurement gas and was also distinguishable at a glance through a polar plot. The device exhibited high detection performance for CH_3COCH_3 , NO_2 , and H_2S gases, with high reproducibility, manufacturing simplicity, and high yield mass production, presenting great potential for various practical applications.

Supplementary Materials: The following are available online at <https://www.mdpi.com/1424-8220/21/5/1922/s1>.

Author Contributions: Conceptualization, Methodology, Software, Validation, Formal analysis, Resources, Writing—original draft, and Visualization. G.S.K.; Conceptualization, Methodology, Validation, and Formal analysis. Y.P.; Methodology, Validation, and Formal analysis. J.S.; Writing—review and editing and Supervision Y.G.S.; Conceptualization, Formal analysis, Writing—original draft, Writing—review and editing, Visualization, Supervision, Funding acquisition, and Project administration. C.-Y.K. All authors have read and agreed to the published version of the manuscript.

Funding: This work was supported by the National Research Council of Science & Technology (NST) grant by the Korean government (MSIP) (No. CAP-17-04-KRISS), the National R&D Program through the National Research Foundation of Korea (NRF) funded by the Ministry of Science and ICT (NRF-2020M3H4A3105594), and an Energy Technology Development Project (KETEP) grant funded by the Ministry of Trade, Industry and Energy, Republic of Korea (2018201010636A) and the Korea Institute of Science and Technology (2E30410).

Institutional Review Board Statement: Not applicable.

Informed Consent Statement: Written informed consent has been obtained from the participants involved in this study.

Data Availability Statement: The data presented in this study are available on request from the corresponding author. The data are not publicly available to protect the privacy of the subjects.

Conflicts of Interest: The authors declare no conflict of interest.

References

1. Dhawan, A.P.; Heetderks, W.J.; Pavel, M.; Acharya, S.; Akay, M.; Mairal, A.; Wheeler, B.; Dacso, C.C.; Sunder, T.; Lovell, N.H.; et al. Current and future challenges in point-of-care technologies: A paradigm-shift in affordable global healthcare with personalized and preventive medicine. *IEEE J. Transl. Eng. Health Med.* **2015**, *3*, 1–10. [[CrossRef](#)] [[PubMed](#)]
2. Van Netten, J.J.; Woodburn, J.; Bus, S.A. The future for diabetic foot ulcer prevention: A paradigm shift from stratified healthcare towards personalized medicine. *Diabetes Metab. Res. Rev.* **2020**, *36*, e3234. [[CrossRef](#)] [[PubMed](#)]
3. Flores, M.; Glusman, G.; Brogaard, K.; Price, N.D.; Hood, L. P4 medicine: How systems medicine will transform the healthcare sector and society. *Pers. Med.* **2013**, *10*, 565–576. [[CrossRef](#)] [[PubMed](#)]
4. Oosthuizen, D.N.; Motaung, D.E.; Swart, H.C. Selective detection of CO at room temperature with CuO nanoplatelets sensor for indoor air quality monitoring manifested by crystallinity. *Appl. Surf. Sci.* **2019**, *466*, 545–553. [[CrossRef](#)]
5. Stefanov, B.I.; Lebrun, D.; Mattsson, A.; Granqvist, C.G.; Österlund, L. Demonstrating online monitoring of air pollutant photodegradation in a 3D printed gas-phase photocatalysis reactor. *J. Chem. Educ.* **2015**, *92*, 678–682. [[CrossRef](#)]
6. World Health Organization. *Air Quality Guidelines for Europe*, 2nd ed.; WHO Regional Publications; World Health Organization, Regional Office for Europe: Copenhagen, Denmark, 2000.
7. Spergel, J.M.; Fogg, M.I.; Bokszzanin-Knosala, A. Correlation of exhaled nitric oxide, spirometry and asthma symptoms. *J. Asthma* **2005**, *42*, 879–883. [[CrossRef](#)]
8. Wang, Z.; Wang, C. Is breath acetone a biomarker of diabetes? A historical review on breath acetone measurements. *J. Breath Res.* **2013**, *7*, 037109. [[CrossRef](#)]
9. Probert, C.S.; Khalid, T.; Ahmed, I.; Johnson, E.; Smith, S.; Ratcliffe, N.M. Volatile organic compounds as diagnostic biomarkers in gastrointestinal and liver diseases. *J. Gastrointest. Liver Dis.* **2009**, *18*, 337–343. [[PubMed](#)]
10. Hakim, M.; Broza, Y.Y.; Barash, O.; Peled, N.; Phillips, M.; Amann, A.; Haick, H. Volatile organic compounds of lung cancer and possible biochemical pathways. *Chem. Rev.* **2012**, *112*, 5949–5966. [[CrossRef](#)]
11. Tremaroli, V.; Bäckhed, F. Functional interactions between the gut microbiota and host metabolism. *Nature* **2012**, *489*, 242–249. [[CrossRef](#)] [[PubMed](#)]
12. Kim, Y.J.; Yu, H.Y.; Baek, I.B.; Ahn, C.G.; Lee, B.K.; Kim, Y.; Yoon, Y.S.; Lim, J.E.; Lee, B.J.; Jang, W.I.; et al. Use of gas-sensor array technology in lung cancer diagnosis. *J. Sens. Sci. Technol.* **2013**, *22*, 249–255. [[CrossRef](#)]
13. Yoon, J.W.; Lee, J.H. Toward breath analysis on a chip for disease diagnosis using semiconductor-based chemiresistors: Recent progress and future perspectives. *Lab Chip* **2017**, *17*, 3537–3557. [[CrossRef](#)]
14. Song, Y.G.; Shim, Y.S.; Suh, J.M.; Noh, M.S.; Kim, G.S.; Choi, K.S. Ionic-activated chemiresistive gas sensors for room-temperature operation. *Small* **2019**, *15*, 1902065. [[CrossRef](#)]
15. Song, Y.G.; Shim, Y.S.; Han, S.D.; Lee, H.R.; Ju, B.K.; Kang, C.Y. Metal oxide nanocolumns for extremely sensitive gas sensors. *J. Sens. Sci. Technol.* **2016**, *25*, 184–188. [[CrossRef](#)]
16. Song, Y.G.; Park, J.Y.; Suh, J.M.; Shim, Y.-S.; Yi, S.Y.; Jang, H.W.; Kim, S.; Yuk, J.M.; Ju, B.-K.; Kang, C.-Y. Heterojunction based on Rh-decorated WO₃ nanorods for morphological change and gas sensor application using the transition effect. *Chem. Mater.* **2018**, *31*, 207–215. [[CrossRef](#)]
17. Miller, D.R.; Akbar, S.A.; Morris, P.A. Nanoscale metal oxide-based heterojunctions for gas sensing: A review. *Sens. Actuators B Chem.* **2014**, *204*, 250–272. [[CrossRef](#)]
18. Gong, B.; Shi, T.; Zhu, W.; Liao, G.; Li, X.; Huang, J.; Zhou, T.; Tang, Z. UV irradiation-assisted ethanol detection operated by the gas sensor based on ZnO nanowires/optical fiber hybrid structure. *Sens. Actuators B Chem.* **2017**, *245*, 821–827. [[CrossRef](#)]
19. Li, W.; Guo, J.; Cai, L.; Qi, W.; Sun, Y.; Xu, J.L.; Sun, M.; Zhu, H.; Xiang, L.; Xie, D.; et al. UV light irradiation enhanced gas sensor selectivity of NO₂ and SO₂ using rGO functionalized with hollow SnO₂ nanofibers. *Sens. Actuators B Chem.* **2019**, *290*, 443–452. [[CrossRef](#)]
20. Jeon, J.M.; Shim, Y.S.; Han, S.D.; Kim, Y.H.; Kang, C.Y.; Kim, J.S.; Kim, M.; Jang, H.W. Vertically ordered SnO₂ nanobamboos for substantially improved detection of volatile reducing gases. *J. Mater. Chem. A* **2015**, *3*, 17939–17945. [[CrossRef](#)]

21. Kang, J.G.; Park, J.S.; Lee, H.J. Pt-doped SnO₂ thin film based micro gas sensors with high selectivity to toluene and HCHO. *Sens. Actuators B Chem.* **2017**, *248*, 1011–1016. [[CrossRef](#)]
22. Suh, J.M.; Shim, Y.-S.; Kwon, K.C.; Jeon, J.-M.; Lee, T.H.; Shokouhimehr, M.; Jang, H.W. Pd-and Au-decorated MoS₂ gas sensors for enhanced selectivity. *Electron. Mater. Lett.* **2019**, *15*, 368–376. [[CrossRef](#)]
23. Choi, S.J.; Ku, K.H.; Kim, B.J.; Kim, I.D. Novel templating route using Pt infiltrated block copolymer microparticles for catalytic Pt functionalized macroporous WO₃ nanofibers and its application in breath pattern recognition. *ACS Sens.* **2016**, *1*, 1124–1131. [[CrossRef](#)]
24. Moon, H.G.; Jung, Y.; Han, S.D.; Shim, Y.S.; Shin, B.; Lee, T.; Kim, J.S.; Lee, S.; Jun, S.C.; Park, H.H.; et al. Chemiresistive electronic nose toward detection of biomarkers in exhaled breath. *ACS Appl. Mater. Interfaces* **2016**, *8*, 20969–20976. [[CrossRef](#)]
25. Han, S.D.; Noh, M.S.; Kim, S.; Shim, Y.S.; Song, Y.G.; Lee, K.; Lee, H.R.; Nahm, S.; Yoon, S.J.; Kim, J.S. Versatile approaches to tune a nanocolumnar structure for optimized electrical properties of In₂O₃ based gas sensor. *Sens. Actuators B Chem.* **2017**, *248*, 894–901. [[CrossRef](#)]
26. Zhou, X.; Xue, Z.; Chen, X.; Huang, C.; Bai, W.; Lu, Z.; Wang, T. Nanomaterial-based gas sensors used for breath diagnosis. *J. Mater. Chem. B.* **2020**, *8*, 3231. [[CrossRef](#)]
27. Hoa, N.D.; Duy, N.V.; Hieu, N.V. Crystalline mesoporous tungsten oxide nanoplate monoliths synthesized by directed soft template method for highly sensitive NO₂ gas sensor applications. *Mater. Res. Bull.* **2013**, *48*, 440–448. [[CrossRef](#)]
28. Volanti, D.P.; Felix, A.A.; Orlandi, M.O.; Whitfield, G.; Yang, D.-J.; Longo, E.; Tuller, H.L.; Varela, J.A. The role of hierarchical morphologies in the superior gas sensing performance of CuO-based chemiresistors. *Adv. Funct. Mater.* **2013**, *23*, 1759–1766. [[CrossRef](#)]
29. Nasiri, N.S.; Clarke, C.T. Nanostructured chemiresistive gas sensors for medical applications. *Sensors* **2019**, *19*, 462. [[CrossRef](#)] [[PubMed](#)]
30. Daryakenari, A.A.; Apostoluk, A.; Delaunay, J.J. Effect of Pt decoration on the gas response of ZnO nanoparticles. *Phys. Status Solidi C* **2013**, *10*, 1297–1300. [[CrossRef](#)]
31. Elias, M.R.; Rotem, V.; Stephane, R. Measurement of temperature and relative humidity in exhaled breath. *Sens. Actuators B Chem.* **2020**, *304*, 127371.
32. Lawryk, N.J.; Liroy, P.J.; Weisel, C.P. Exposure to volatile organic compounds in the passenger compartment of automobiles during periods of normal and malfunctioning operation. *J. Expos. Anal. Environ. Epidemiol.* **1995**, *5*, 511–531.
33. Tom, A.; Tomas, E.; Ingemar, L.; Per, M. Drift correction for gas sensors using multivariate methods. *J. Chemom.* **2000**, *14*, 711–723.
34. Alice, C.; Sabato, M.; Marco, C. An exploratory factor analysis of sensor-based physical capability assessment. *Sensors* **2019**, *19*, 2227.
35. Alexander, S.; Vikram, J.; Sergei, S. Gas sensor array based on metal-decorated carbon nanotubes. *J. Phys. Chem. B* **2006**, *110*, 42.
36. Sanchez, C.; Santos, P.; Lozano, J. Use of electronic noses for diagnosis of digestive and respiratory diseases through the breath. *Biosensors* **2019**, *9*, 35. [[CrossRef](#)]
37. Wilson, A.D. Applications of electronic-nose technologies for noninvasive early detection of plant, animal and human diseases. *Chemosensors* **2018**, *6*, 45. [[CrossRef](#)]